Pergamon

Int. J. Heat Mass Transfer. Vol. 39, No. 2, pp. 299–310, 1996

0017–9310/96 $9.50+0.00

0017–9310(95)00120–4

Developing three-dimensional laminar mixed convection in a circular tube inserted with longitudinal strips

SHOU-SHING HSIEH and MAO-YU WEN

Department of Mechanical Engineering, National Sun Yat-Sen University, Kaohsiung, Taiwan 80424, Republic of China

(*Received* 26 *October* 1994 *and in final form* 10 *March* 1995)

Abstract—A finite-difference numerical study with a boundary-fitted coordinate system was made to investigate the three-dimensional, steady-state, laminar entrance flow of an axially uniformly heated horizontal tube with different adiabatic inserts. Parametric calculations have been performed to determine the nature and effect on thermally driven secondary flows of Reynolds number ($100 \leqslant Re \leqslant 1000$), Grashof number ($10^3 \leqslant Gr \leqslant 10^6$), aspect ratio ($1 \leqslant AR \leqslant 8$) and radius ratio ($0 \leqslant R^* \leqslant 1$). Typical streamline patterns, isotherms and axial velocity along the flow direction are obtained. Local friction factor, Nusselt number and entrance length in the hydrodynamically and thermally developing, and fully developed regions are presented and discussed. Furthermore, flow visualization was made and compared with the corresponding numerical results. The agreement is good for $Re = 500$ at the two different downstream distances.

1. INTRODUCTION

Convective heat transfer in horizontal ducts is frequently encountered in many engineering applications, particularly for the design of heat exchangers. A comprehensive review of forced convection in ducts had been reported by Shah and Bhatti [1]. It has long been recognized that the presence of buoyancy would significantly affect the laminar forced convection in horizontal ducts due to the induced secondary flow, which enhances heat transfer between the wall and the fluid.

As a practically used displaceable device, a longitudinal rectangular plate is often inserted in the tubes of heat exchangers to enhance tubeside heat transfer. Recently, Solanki *et al.* [2, 3] conducted experimental and theoretical studies on laminar forced convection in tubes with polygonal inner cores. Chen and Hsieh [4] numerically studied laminar mixed convection in a horizontal tube with a longitudinal square core.

Most studies in the literature were concerned with fully developed conditions, however it was unclear how the flow develops to the final states for laminar mixed convection in a horizontal tube, especially with a longitudinal strip in its core. The developing process would not only provide insight into the complicated physics involved, but also legitimize the fully developed solution. Moreover, literature on developing three-dimensional (3-D) laminar mixed convection tube flow with a longitudinal insert is relatively scarce.

The present paper is a continuation of the work by Chen and Hsieh [4, 5] on fully developed laminar mixed convection in a horizontal tube with a longitudinal square or rectangular core of aspect ratio 5. It was found that the flow and heat transfer characteristics were affected by the aspect ratio and insert tilt angles (0, 45 and 90°). The purpose of this paper is to shed further light on the development of the primary/secondary flow in the presence of longitudinal squares and rectangular inserts, and their effects on heat transfer and friction characteristics. A clear picture of this developing process will also validate the fully developed solutions. To accomplish this, parabolization of the 3D Navier–Stokes equation in the streamwise direction was employed. Although this approximation is valid only for small Grashof numbers without flow reversal, the present solution for $10^{-3} \leqslant Gr/Re^2 \leqslant 10^2$ can still reveal adequate flow phenomena for what one would like to examine. The SIMPLE algorithm of Patankar [6] with the slight modification of having the velocity and pressure as well as energy fields satisfy global continuity at every streamwise location was implemented with the body-fitted coordinate system.

2. THEORETICAL ANALYSIS

The problem of the steady, developing, laminar mixed convection flow in an axially, uniformly heated horizontal tube with different longitudinal inserts as illustrated in Fig. 1 is considered. A uniform inlet axial velocity W_m and a constant inlet temperature, t_{in}, are imposed at $Z = 0$. It is assumed that the thermophysical properties are constant except for the density in the buoyancy term. Axial diffusion [due to a large Pelect number under study (say, $Pe > 100$)], viscous

NOMENCLATURE

A_f dimensionless flow area of the passage
AR aspect ratio for the present study, L/H
d_h hydraulic diameter [m]
g gravitational acceleration [m s^{-2}]
Gr Grashof number, $\beta g q_{in} d_h^4/kv^2$
H dimensionless height of insert, h/R_o
J Jacobian of the transform
k thermal conductivity of fluid [W m^{-1} K^{-1}]
L dimensionless width of insert, l/R_o
L_h entrance length [m]
L_h^+ dimensionless entrance length, $L_h/(d_h\, Re\, Pr)$
N dimensionless normal direction
Nu sectional averaged Nusselt number of heated tube
$\bar{p}$ average pressure over the cross-section at each axial location [kg m^{-2}]
P outer parameter [m]
$\bar{P}$ dimensionless cross-sectionally mean pressure, $\bar{p}/\rho W_m^2$
Pr Prandtl number, v/α
P_o dimensionless outer parameter
q_{in} prescribed averaged heat flux on outer tube [W m^{-2}]
R source term of governing equation
R^* radius ratio of circumscribed circle of insert to outer tube, $0.5(L^2+H^2)^{1/2}$
Re Reynolds number based on W_m, $W_m d_h/v$
RN normalized radial distance, $(\eta-\eta_{min})/(\eta_{max}-\eta_{min})$
R_o radius of outer tube [m]
t temperature
T dimensionless temperature, $(t-t_s)/(q_{in}d_h/k)$
t_b bulk temperature, $\iint wtJ\,dx\,dy/\iint wJ\,dx\,dy$ [K]
T_b dimensionless bulk temperature, $(t_b-t_s)/(q_{in}d_h/k) = \iint WTJ\,dX\,dY/\iint WJ\,dX\,dY$
T_m dimensionless inlet temperature, $(t_{in}-t_s)/(q_{in}d_h/k)$
t_s surface temperature at outer wall [K]
u, v, w velocity components in the x-, y-, z-directions [m s^{-1}]
U, V, W dimensionless velocity component in the X-, Y-, Z-directions
W_m maximum axial velocity [m s^{-1}]
x, y, z rectangular coordinates [m]
X, Y, Z dimensionless rectangular coordinates
Z^+ dimensionless distance in the main flow direction, $Z/(d_h\, Re\, Pr)$.

Greek symbols
α thermal diffusivity of fluid [m^2 s^{-1}]
β coefficient of thermal expansion of fluid [K^{-1}]
θ angular position [°]
ν kinematic viscosity of fluid [m^2 s^{-1}]
ξ, η dimensionless coordinates in transformed domain
ρ density [kg m^{-3}]
ϕ generalized variable.

Subscripts
f fully developed quantity
in inlet quantity
max maximum value
min minimum value.

dissipation (for low speed) and compressibility effects are neglected. The fluid is Newtonian.

Subject to these assumptions, the governing dimensionless equations can then be written as follows:

$$\frac{\partial U}{\partial X}+\frac{\partial V}{\partial Y}+\frac{\partial W}{\partial Z}=0 \tag{1}$$

$$U\frac{\partial U}{\partial X}+V\frac{\partial U}{\partial Y}+W\frac{\partial U}{\partial Z}=-\frac{\partial \bar{P}}{\partial X}+\frac{1}{Re}\left(\frac{\partial^2 U}{\partial X^2}+\frac{\partial^2 U}{\partial Y^2}\right) \tag{2}$$

$$U\frac{\partial V}{\partial X}+V\frac{\partial V}{\partial Y}+W\frac{\partial V}{\partial Z}=-\frac{\partial \bar{P}}{\partial Y}+\frac{1}{Re}\left(\frac{\partial^2 V}{\partial X^2}+\frac{\partial^2 V}{\partial Y^2}\right)+\frac{Gr}{Re^2}T \tag{3}$$

$$U\frac{\partial W}{\partial X}+V\frac{\partial W}{\partial Y}+W\frac{\partial W}{\partial Z}=-f(Z)+\frac{1}{Re}\left(\frac{\partial^2 W}{\partial X^2}+\frac{\partial^2 W}{\partial Y^2}\right) \tag{4}$$

$$U\frac{\partial T}{\partial X}+V\frac{\partial T}{\partial Y}+W\frac{\partial T}{\partial Z}+\frac{\Psi W}{Pr\,Re}=\frac{1}{Pr\,Re}\left(\frac{\partial^2 T}{\partial X^2}+\frac{\partial^2 T}{\partial Y^2}\right) \tag{5}$$

where

$$\Psi=\frac{P_o}{W_m A_f}.$$

The equations are non-dimensionalized in terms of the following dimensionless quantities:

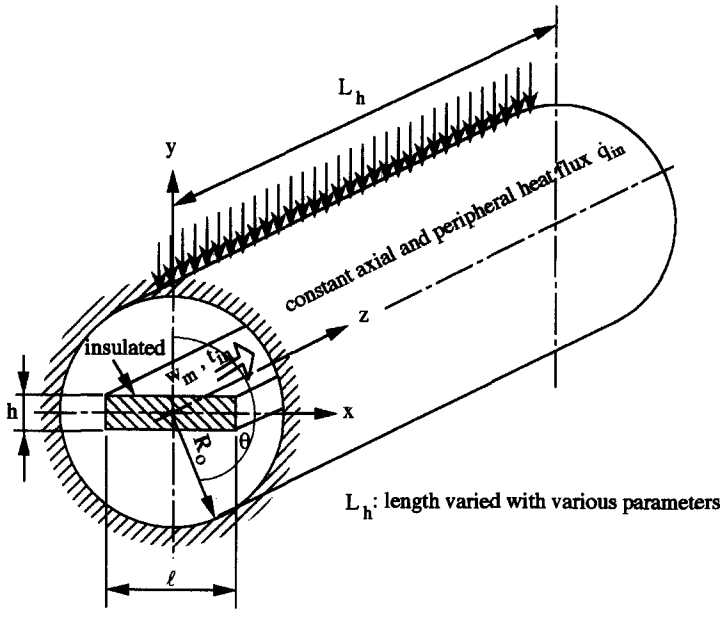

Fig. 1. Schematic diagram for the present physical system.

$$X=\frac{x}{d_h} \quad Y=\frac{y}{d_h} \quad Z=\frac{z}{d_h} \quad U=\frac{u}{W_m} \quad V=\frac{v}{W_m}$$

$$W=\frac{w}{W_m} \quad T=\frac{t-t_s}{q_{in}d_h/k} \quad \bar{P}=\frac{\bar{p}}{\rho W_m^2} \quad P_o=\frac{P}{d_h}.$$

The boundary conditions are expressed as

$$U=V=0 \quad W=1 \quad T=T_m \quad \text{at } Z=0$$

$$U=V=W=0 \quad \frac{\partial T}{\partial N}=0 \quad \text{at insert}$$

$$U=V=W=0\ T=0 \quad \text{at tube wall.}$$

Upon simplification and due to the present geometry, it can be seen that there are five dimensionless parameters displayed in the following for the present study:

(1) aspect ratio for the present insert, $AR=L/H$;
(2) radius ratio, $R^*=0.5(L^2+H^2)^{1/2}$;
(3) Prandtl number, $Pr=\nu/\alpha$;
(4) Reynolds number, $Re=W_m d_h/\nu$;
(5) Grashof number, $Gr=\beta g q_{in} d_h^4/(k\nu^2)$.

In addition, the term of Gr/Re^2, known as a measure of relative contributions of buoyancy force to inertia force, was also used in the present study.

The axial gradient of the cross-sectionally mean pressure may be decoupled by making the usual parabolic assumption reported by Patankar and Spalding [7]. It is then given by

$$-\frac{d\bar{P}}{dZ}=-f(Z) \tag{6}$$

where $f(Z)$ is determined by the constraint for the constant flow rate. This additional constraint is expressed as

$$\iint W\,dX\,dY=A_f. \tag{7}$$

Following the general definition, the friction factor, f, and local outer wall Nusselt number, Nu, can be derived as follows:

$$f=\frac{1}{2}\left(-\frac{d\bar{P}}{dZ}\right) \tag{8}$$

$$Nu=-\frac{1}{T_b} \tag{9}$$

where T_b is the dimensionless bulk temperature, which is defined as:

$$T_b=\frac{\iint WTJ\,dX\,dY}{\iint WJ\,dX\,dY}.$$

3. NUMERICAL PROCEDURE

The 3D, governing equations can typically be written in Cartesian coordinates for the dependent variable ϕ in the following form:

$$\frac{\partial}{\partial X}(U\phi)+\frac{\partial}{\partial Y}(V\phi)+\frac{\partial}{\partial Z}(W\phi)=\frac{\partial}{\partial X}\left(\Gamma\frac{\partial\phi}{\partial X}\right)+\frac{\partial}{\partial Y}\left(\Gamma\frac{\partial\phi}{\partial Y}\right)+R(X,Y,Z). \tag{10}$$

The parameters in equation (10) are defined in Table 1.

Adopting the body-fitted coordinate systems developed by Thompson *et al.* [8] with new inde-

Table 1. Definition of parameters in equations (10) and (11)

Equations	ϕ	Γ	$R(X, Y, Z)$
Physical domain			
Continuity	1	1	0
Momentum	U	$\frac{1}{Re}$	$-\frac{\partial \bar{P}}{\partial X}$
	V	$\frac{1}{Re}$	$-\frac{\partial \bar{P}}{\partial Y}+\frac{Gr\,T}{Re^2}$
	W	$\frac{1}{Re}$	$-f(Z)$
Energy	T	$\frac{1}{Pr\,Re}$	$-\frac{\Psi W}{Pr\,Re}$
Transformed domain			
Equations	ϕ	Γ	$R(\xi, \eta, Z)$
Continuity	1	1	0
Momentum	U	$\frac{1}{Re}$	$Y_\zeta P_\eta - Y_\eta P_\zeta$
	V	$\frac{1}{Re}$	$-J\frac{Gr\,T}{Re^2}-X_\zeta P_\eta + X_\eta P_\zeta$
	W	$\frac{1}{Re}$	$-Jf(Z)$
Energy	T	$\frac{1}{Pr\,Re}$	$-J\frac{\Psi W}{Pr\,Re}$

pendent variables $\xi(X, Y)$ and $\eta(X, Y)$, a schematic illustration of the relationship between the physical domain and the transformed domain shown in Fig. 2 can be rewritten as follows:

$$\frac{\partial}{\partial \xi}(\bar{U}\phi)+\frac{\partial}{\partial \eta}(\bar{V}\phi) + J\frac{\partial}{\partial Z}(W\phi)=\frac{\partial}{\partial \xi}\left[\frac{\Gamma}{J}\left(\alpha\frac{\partial \phi}{\partial \xi}-\beta\frac{\partial \phi}{\partial \eta}\right)\right] + \frac{\partial}{\partial \eta}\left[\frac{\Gamma}{J}\left(\gamma\frac{\partial \phi}{\partial \eta}-\beta\frac{\partial \phi}{\partial \xi}\right)\right]+R(\xi, \eta, Z) \quad (11)$$

where $\alpha = X_\eta^2 + Y_\eta^2$, $\beta = X_\xi X_\eta + Y_\xi Y_\eta$, $\gamma = X_\xi^2 + Y_\xi^2$, $J = X_\xi Y_\eta - X_\eta Y_\xi$ and $\bar{U} = UY_\eta - VX_\eta$, $\bar{V} = -UY_\xi + VX_\xi$.

These relations may then be inverted to obtain

$$U = \bar{U}\frac{X_\xi}{J} + \bar{V}\frac{X_\eta}{J} \quad V = \bar{V}\frac{Y_\eta}{J} + \bar{U}\frac{Y_\xi}{J}. \quad (12)$$

The source term $R(\xi, \eta, Z)$ in the $\xi-\eta-Z$ coordinates is also given in Table 1.

According to Thompson *et al.* [9], all Dirichlet boundary conditions must remain in the same in the transformed plane. At the inner wall, the boundary condition for the temperature becomes

$$\left.\frac{\partial T}{\partial \eta}\right|_s = \left.\frac{\partial T}{\partial N}\right|_\eta \frac{J}{\sqrt{\gamma}} + \left.\frac{\beta}{\gamma}\frac{\partial T}{\partial \xi}\right|_s \quad \text{at insert} \quad (13)$$

A 41×21 boundary-fitted grid in the physical domain, shown in Fig. 2, has more grid lines closely packed near both walls. On the other hand, at the inlet of the entrance region, the variation of variables near the walls along the axial direction is large. Consequently, a very small axial step in the upstream is required for accuracy. By means of many tests for the axial grid lines, the finest grid is located adjacent to the entrance, and the sizes of other grids are chosen such that each is within 125% of the adjacent grid (based on a trial and error procedure) in order to avoid abrupt changes and to obtain convergence.

Due to the similarity between equations (10) and (11), the major steps of the SIMPLE solution procedure developed by Patankar [6], which has been used successfully for flow calculation in Cartesian coordinates, can be extended to fit the coordinate system after some modifications. The numerical procedure is as follows.

(1) The initial values of the unknowns U, V, $\bar{U}$ and $\bar{V}$ are assigned to be zero at the entrance, $Z = 0$. Uniform inlet axial velocity, $W = 1$, and a constant inlet temperature, $T = 0$, are used.

(2) The transformation coefficients α, β, γ and the Jacobian of the transformation J are determined by the transformed Boussinesq equations reported by Thompson *et al.* [9]. These coefficients and Jacobian are computed at each point and return to the main program by the grid-generating subprogram.

(3) Applying the boundary conditions and the known values of variables for U, V, W, $\bar{U}$, $\bar{V}$, T and $f(Z)$ at the beginning position in the momentum equations (11) and (12), the new values of U, V, W and $f(Z)$ at the interior points of the next axial position are obtained, by power law scheme, with constraint (7) for constant flow rate. In this step the pressure correction equation and the velocity corrections are used.

(4) With the newly obtained values for U, V, W at step 3, the energy equation (11) can be solved iteratively for the interior temperature subject to the boundary condition (13).

(5) Return to step 3 and continue until the following criteria of convergence for U, V, W and T are satisfied at a cross-section

$$\text{Max}\,|F_{i,j}^{(n+1)} - F_{i,j}^{(n)}|/\text{Max}\,|F_{i,j}^{(n+1)}| < 10^{-5}$$

where n is the nth iteration of steps 3 and 4.

(6) The angular local friction factor-Reynolds number product, fRe is calculated from equation (8).

(7) The local outer wall Nusselt numbers are determined from equation (9).

(8) Steps 3–7 are repeated at the next axial location until the final Z location is reached.

4. ACCURACY OF THE SOLUTION

The numerical calculations in this study were performed for laminar mixed convection in a horizontal tube with various different longitudinal inserts. Following Chen and Hsieh [4], the aspect ratio for the present geometry, A ($= L/H$), of 0–10, and the radius ratio of circumscribed circle of insert to outer tube,

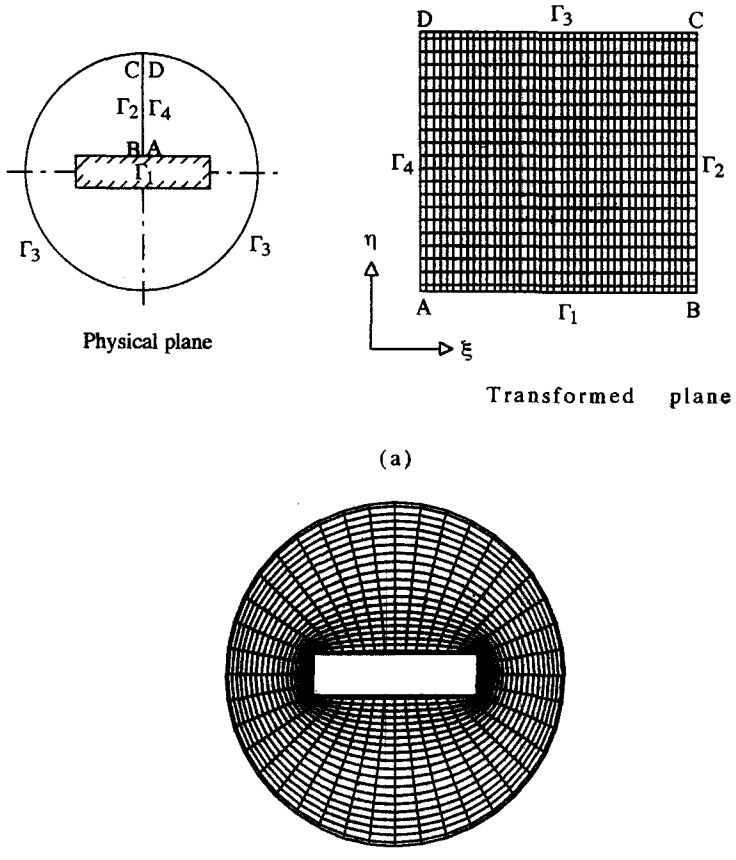

Fig. 2. (a) Transformation of the solution domain. (b) The body-fitted coordinate system.

R^* $(= 0.5(L^2+H^2)^{1/2})$, of 0–1 were applied. Air ($Pr \approx 0.7$) was used in this study. To avoid possible occurrences of flow reversal and transition (see ref. [10]) and to assure a fully developed condition could eventually be reached in mixed convection duct flow, the numerical simulations were considered for $0 \leqslant Gr \leqslant 10^6$ at $100 \leqslant Re \leqslant 1000$. The accuracy of the numerical solution and the computing time depend on the spanwise and streamwise grid spacings, while the range of spanwise meshes depends on the values of AR and R^*. If ΔZ^+ is chosen small enough, only one or two iterations are needed before marching downstream to the next X–Y plane. The axial step sizes, ΔZ^+, varying from 10^{-5} near the entrance to 10^{-2} near the fully developed region, are found to be satisfactory. This results in approximately 2150 axial steps in each run. Great care was taken near the entrance since at a higher Gr the onset of secondary flow occurs sooner. The effect of mesh size for a certain case is shown in Fig. 3. It is found that the 21×15 and 31×19 meshes are too coarse to provide grid-independent results, however the computations with the 41×21 and 61×31 meshes yielded almost identical results (within a 0.2% change). In addition, the numerical

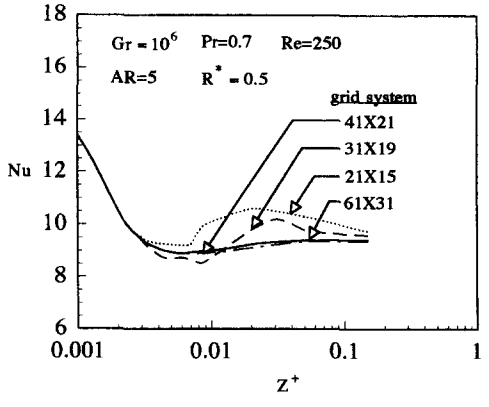

Fig. 3. Nusselt number distributions with various mesh sizes.

scheme (41×21 mesh) was also demonstrated to satisfy the governing difference equations to a maximum deviation within 1%. In order to save computing time, the 41×21 mesh was accordingly employed. The mesh sizes used in the final computation and the typical computing time required on a supercomputer in obtaining a complete result for

Table 2. Numerical experiments for grid size and computing times

R^*	AR	M_1	M_2	M	N	cpu [s]
0.0		NA		51	27	3100
0.0–0.3	1 2 5 8	$M = 2+(4M_1+2M_2)$		≈ 45	25	≈ 4800
0.3–0.7	1 2 5 8	$M = 2+(4M_1+2M_2)$		≈ 41	21	≈ 4200
0.7–1.0	1 2 5 8	$M = 2+(4M_1+2M_2)$		≈ 51	13	≈ 3900
1.0	1 2 5 8	$M = 2+(4M_1+2M_2)$		≈ 61	11	≈ 4100

NA, not available; $R^* = 0.5\sqrt{(H^2+L^2)}$; $AR = L/H$.

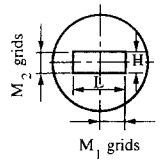

the axial distance ΔZ^+ ranging from 10^{-5} to 10^{-2} with a given range of Gr are given in Table 2.

To facilitate the presentation of the secondary flow pattern, a dimensionless cross-sectional stream function ψ is so defined as to be calculated from the velocity components by $\psi = \int_{\eta_i}^{\eta} U_\xi \, d\eta$ with $\psi = 0$ at $\eta = \eta_i$ (insert wall). Table 3 depicts the parameters considered in the present study.

5. RESULTS AND DISCUSSION

Based on hydrodynamic considerations, the flow field is significantly influenced by the present insert blockage and the secondary flow circulation. The insert increases the wetted perimeter and reduces the flow cross-sectional area. The secondary circulation due to buoyancy, which causes a transverse flow across the nearly partitioned tube cross-section, is quantitatively shown in Figs. 4 and 5.

The developing process can be better illustrated from the typical crossflow patterns: crossflow streamlines and isotherms. Here, unless stated otherwise, the contours are drawn at equal increments and the reference values are given at the bottom of each figure. Figure 4(a)–(f) shows the two-vortex result (only one counterclockwise vortex is shown due to the nature of symmetry) of $Pr = 0.7$ for $Gr/Re^2 \cong 0.16$ at six different downstream locations with a square insert. At $Z^+ = 5 \times 10^{-4}$ shown in Fig. 4(a), which is approximately only one-eighth of the diameter of the tube, the buoyancy driven secondary flow has already been noted, but it is still weak, especially near the insert and tube boundary. The phenomenon is still local in nature and the occurrence of plumes in the upper/lower half is similarly due to the growth of the boundary layer.

Table 3. Relevant parameters considered in the present study

AR	1, 2, 5, 8
Gr	$10^3, 10^4, 10^5, 10^6$
Re	$100 \leqslant Re \leqslant 1000$
$\frac{Gr}{Re^2}$	$1.0\times10^{-3} \leqslant \frac{Gr}{Re^2} \leqslant 1.0\times10^{2}$

Since the fluid is uniformly circumferentially heated in the tube, the fluid near the outer wall is warmer than the bulk fluid in the core. As a consequence, two upward currents flow along half of the side walls and, by continuity, the heavier fluid near the center of the tube flows downwards in Fig. 4. Furthermore, due to the adiabatic square plate inserted concentrically in the present tube, two sets of spiralling vortices which are symmetrical about a vertical midplane were formed. The corresponding location and size of these vortices do not appear to have changed substantially at different axial downstream distances. This is because the constraint of both the narrow and the annulus space for the present tube with the adiabatic square plate suppressed the movement of the vortices. The temperature pattern shown in the left portion of Fig. 4(a) suggests that the crossflow is mostly conductive which strongly indicates the axial velocity (W)

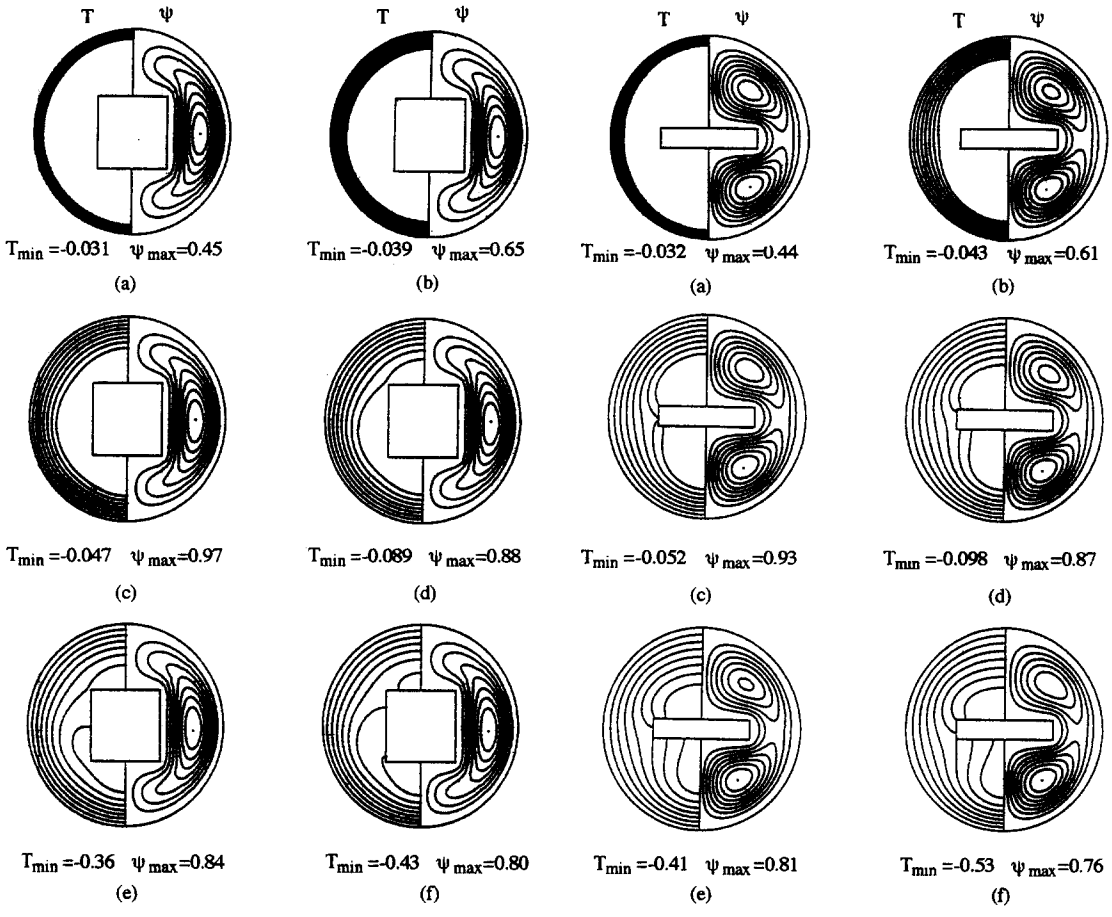

Fig. 4. Development of streamline pattern (right) and isotherms (left) in a horizontal tube with a longitudinal square insert for $Gr/Re^2 = 0.16$ at: (a) $Z^+ = 0.0005$; (b) $Z^+ = 0.005$; (c) $Z^+ = 0.01$; (d) $Z^+ = 0.05$; (e) $Z^+ = 0.1$; (f) $Z^+ = 0.5$ (fully developed).

Fig. 5. Development of streamline patterns (right) and isotherms (left) in a horizontal tube with a longitudinal rectangular insert for $Gr/Re^2 = 0.16$ at: (a) $Z^+ = 0.0005$; (b) $Z^+ = 0.005$; (c) $Z^+ = 0.01$; (d) $Z^+ = 0.05$; (e) $Z^+ = 0.1$; (f) $Z^+ = 0.5$ (fully developed).

has a predominant behavior of forced convection. This can also be verified in the following discussion. As Z^+ increases to $Z^+ = 5 \times 10^{-2}$ [Fig. 4(c)] the secondary flow becomes stronger. This is because the colder fluid in the core region moves downwards to fill the void and a clear vortical flow pattern emerges. It is clearly seen that the value of the maximum stream function at any given cross-section increases gradually from the value zero at the entrance $Z^+ = 0$ to a maximum value at certain distance ($Z^+ = 5 \times 10^{-2}$) from the entrance and then decreases thereafter along the axial direction until the flow is thermally fully developed. Moreover, since the buoyancy effect is weak in Fig. 4(a), the isotherms near the side wall are packed closely. In addition, the isotherms for smaller values of T in the central core are not shown due to a nearly uniform temperature there. The distortion of the isotherms near the insert is gradually increased which can clearly be seen from Fig. 4(b)–(f) in the further downstream distance due to the buoyancy effect. Taking a closer examination of Fig. 4, it also indicates that the movement of the isotherms near the insert in the bottom is faster than that in the top. This is because the ψ_{max} of the vortex in the bottom is higher than that in the top [these can be seen in Fig. 4 (right)].

Isotherms and streamlines predicted in a horizontal tube with a longitudinal square insert for the different streamwise distance are shown in Fig. 5(a)–(f). Unlike the square insert in Fig. 4, the circulation shown in Fig. 5 breaks up into two symmetric corotating vortices which are supposedly connected through a saddle point. Again, the location and size of the vortex do not appear to change substantially for all the figures [Fig. 5(a)–(f)], however there is a rapid change in ψ_{max} in the flow pattern as Z^+ increases. This can be seen from the variation of ψ_{max} values [see Fig. 5(a)–(f) (right)]. On the other hand, the thermal field is fairly stratified in the circumference in most of the flow domain. This behavior persists until $Z^+ = 0.1$ [Fig. 5(e)] where the buoyancy effect is significant. Close examination of Fig. 5(a)–(f) shows that the ψ_{max} of the flow pattern with the square insert is higher than that of the corresponding figure with the rectangular

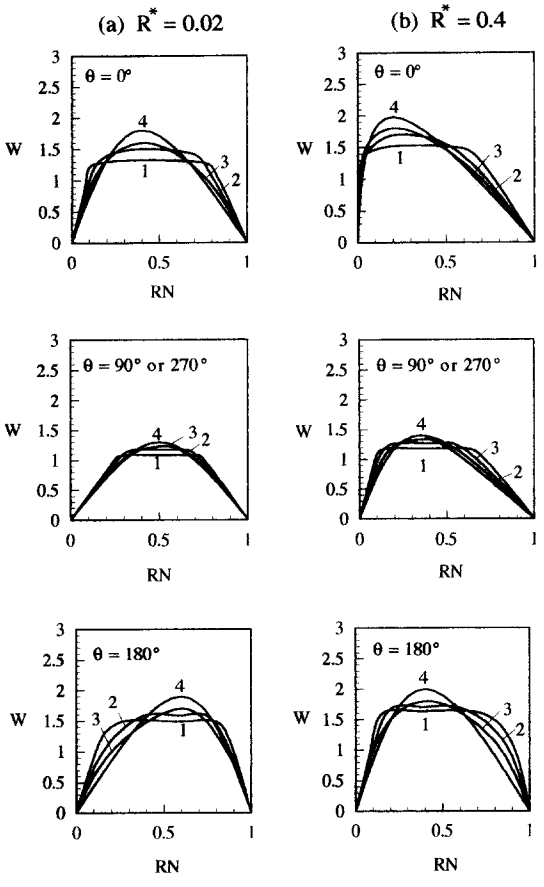

Fig. 6. Development of dimensionless axial velocity profiles vs RN for $Pr = 0.7$, $Re = 250$, $Gr = 10^4$ and $AR = 4$ at different angular positions and streamwise distance: (1) $Z^+ = 0.005$; (2) $Z^+ = 0.01$; (3) $Z^+ = 0.05$; (4) Z^+ = fully developed.

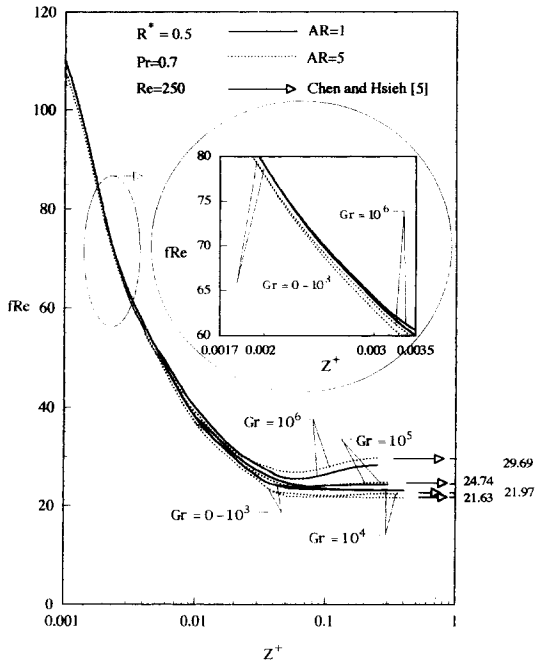

Fig. 7. The local fRe factor vs streamwise distance.

insert, which suggests the former has a stronger secondary motion. However, due to the four-vortex flow pattern shown in the latter case, the mixing is higher and it results in a higher heat transfer, even though it is not clearly noted until $Z^+ = 5 \times 10^{-2}$ because the growing thermal boundary layer from the upper/lower half counterbalances the heat transfer until the mixing is fully accomplished.

The development of axial velocity in the radial direction at some angular locations for both the $R^* = 0.02$ and 0.4 is given in Fig. 6 in which a symbol RN denotes the normalized (with respect to the gap clearance) radial distance in each angular location, with $RN = 0$ for the insert and $RN = 1$ for the tube. It can be seen clearly that the asymmetry in the axial velocity profiles increases as R^* increases. For $R^* = 0.02$ in Fig. 6, near the center, the very small core tube has a large effect on the velocity profile because of the zero velocity boundary condition on the wall, while near the outer wall the profiles are nearly identical. Again, it is seen that the buoyancy effects are significant at a certain distance $Z^+ (\approx 5 \times 10^{-2})$. The buoyancy effect decelerates the fluids near the insert at locations with small gap clearance ($R^* = 0.02$), but accelerates those at locations with large gap clearance ($R^* = 0.4$). This is because the fluids at $R^* = 0.02$ have low kinetic energy in forced convection, and can barely overcome the additional flow resistance by buoyant force, thus they are further decelerated. As a result of the constraint of constant cross-sectional mass flow, velocities at $R^* = 0.4$ must eventually increase and the location of the maximum axial velocity shifts towards the insert at $R^* = 0.4$ and there is an overshoot region as Z^+ increases. A similar overshoot at $Z^+ > 0.01$ for $R^* = 0.02$ was also observed, but the magnitude was less. This is because the upward movement of the high momentum fluid in the core region near the insert makes the maximum axial velocity occur near the insert; the flow in the vicinity of the insert accelerates while that in the rest area decelerates, especially for the core of $R^* = 0.4$. The final fully developed shape of the profile in Fig. 6 at different angular positions for $R^* = 0.02$ and 0.04 with the global maximum shifted away from the line of symmetry corresponds to that of the foregoing four-vortex and two-vortex flow pattern observations, respectively, and they are also assessed further.

Friction factors fRe with streamwise distance for $AR = 1$ and 5 are shown in Fig. 7. In order to investigate the characteristics between the friction factors and the various parameters in detail, part of the original drawing shown in Fig. 7 is enlarged. It is seen that the friction factor behavior at $Gr \leqslant 10^3 (Gr/Re^2 \leqslant 0.016)$ follows the results for pure forced convection. At $Z \cong 5 \times 10^{-2}$, the friction factor starts to deviate from the forced convection value seen in Fig. 7. This onset position seems to occur earlier as Gr increases in

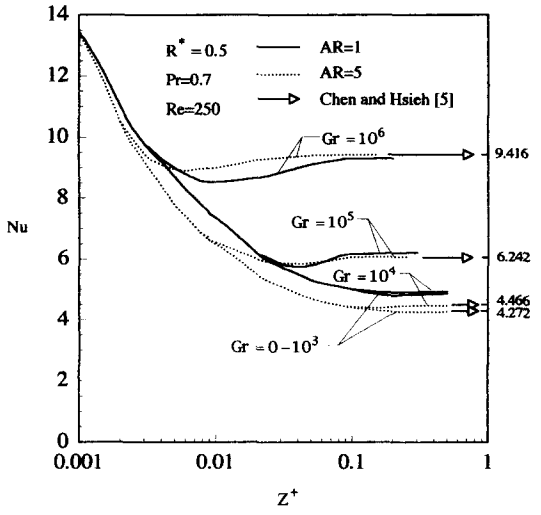

Fig. 8. Local Nusselt number vs streamwise distance.

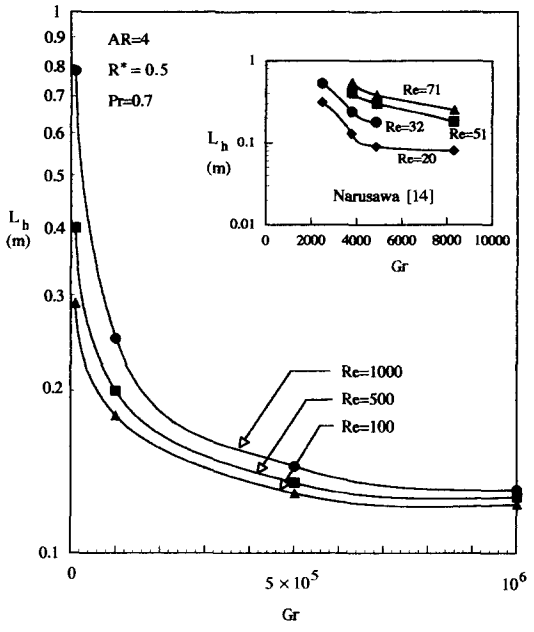

Fig. 9. The variations of L_h(95% Nu_f) with Gr for different Res and a comparison with ref. [14].

which the friction factor is enhanced by the secondary flow due to the buoyancy force. This is strongly suggested even though $Gr/Re^2 < 0.1$, which conventionally indicates the emergence of mixing convection. The buoyancy effect shares its contribution in the heat transfer mechanism and, consequently, this also reflects the importance of buoyancy in developing flow in horizontal tubes. Moreover, it is also noted that the friction factor increases with increasing Gr as one would expect. Upon further inspection of Fig. 7, because the blockage effect becomes more evident, the friction factor increases as AR decreases at the same R^*. However, the buoyancy effects become significant after a certain distance Z^+ is reached, and meanwhile the friction factor increases as AR increases. This may be due to the buoyancy force increasing the drag force of the surface. Finally, after Z^+ is increased to a certain distance, a nominally constant friction factor is reached, and it can be referred to as the fully developed value. These results are in good agreement with those obtained by Chen and Hsieh [5] for fully developed solutions.

Figure 8 shows the buoyancy effects on the local Nusselt number in the entrance region of a horizontal tube with longitudinal square and rectangular inserts for both $AR = 1$ and 5, respectively. It is found that the buoyancy effects are practically negligible. From then on Nu decreases uniformly as it behaves in pure forced convection. The first sign of the buoyancy effect appears in the plot as a local minimum near $Z^+ = 2 \times 10^{-3}$–5×10^{-3}. This region coincides with the points where the secondary flow loses its upward momentum. At this stage, the local fluid is replaced by the lower momentum fluid flow from below. Consequently, the axial velocity is reduced along with Nu. Since the vortex moves upward and gathers strength as it travels further downstream, evidenced by the preceding discussion, the position of the local minimum in Nu moves upstream and the valley becomes deeper as Gr increases. Thereafter, prior to the fully developed condition, the flow near the bottom accelerates due to the momentum transfer by the secondary flow which also reduces the tube surface temperature and, in turn, raises Nu. This behavior becomes stronger as Gr increases. This phenomenon coincided with Nu variations in the entrance region reported by Abou-Ellail and Morcos [12] and Choi and Chi [13]. The relative contributions of forced and natural convection are clearly noted for $0.16 \leqslant Gr/Re^2 \leqslant 16$, especially for $Gr/Re^2 = 16$ at which the natural convection shares almost equal importance with that of forced convection in the fully developed state. Moreover, a similar variation of the fRe plot of Nu along the streamwise distance with an increase in AR was also seen in Fig. 8. Again, excellent agreement of the fully developed Nu is found with Chen and Hsieh [5].

To understand the locations of L_h in relation to the heat transport, the L_hs (95% Nu_f) are obtained for the location where 95% of the Nusselt number of a fully developed flow is reached. Figure 9 shows that the variation of L_h (95% Nu_f) becomes small as Gr increases, which is roughly the same in magnitude over the range of the Gr in the present study. In addition, for a given Gr value the L_h (95% Nu_f) increases as Re increases. It is also seen that the L_hs (95% Nu_f) for the different Res gradually become identical as Gr increases. Also, it is found that the results of L_h (95% Nu_f) are in good agreement qualitatively with those based on the mixed convection at the entrance region of a rectangular duct heated from below [14]. Furthermore, the results of L_h (95% Nu_f) for the lower Re and Gr depicted in Table 4 show good agreement with ref. [14]. The present values of L_h (95% Nu_f) are slightly lower than the corresponding data of Narusawa [14]. This is attributed

Table 4. Comparison with Narusawa [14] for entrance length L_h (95% Nu_f) subjected to lower Re and Gr

Gr	Re	L_h (95% Nu_f) [m] (present study)	L_h (95% Nu_f) [m] (Narusawa [14])
3800	20	0.12	0.14
	50	0.30	0.36
	70	0.41	0.50
4900	20	0.08	0.10
	50	0.21	0.27
	70	0.30	0.37
8300	20	0.06	0.07
	50	0.18	0.21
	70	0.24	0.28

Physical geometry

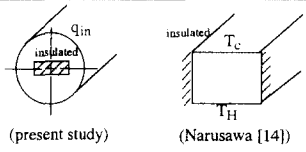

(present study) (Narusawa [14])

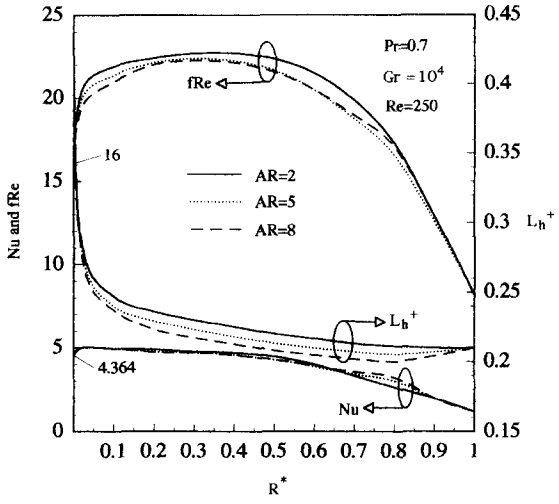

Fig. 10. Nu, fRe and L_h^+ vs R^* for fully developed laminar flow.

to the present geometry which enhances the heat transfer between the wall and the fluid.

Figure 10 compares the R^* dependencies of the fRe factor, Nu and L_h^+ obtained by the present calculation for three different ARs. It can be seen clearly that fRe and Nu increase as R^* increases until R^* equals about 0.5. Then, fRe and Nu decrease as R^* increases. One limiting case of annular ducts, $R^* = 0$, is a circular duct with an 'infinitesimal thickness rectangular insert' at the center. Hence, the boundary conditions for the annular duct with $R^* = 0$ are not identical to those for a general circular duct. However, fortunately, in most cases the flow ($fRe = 16$) and heat transfer ($Nu_f = 4.364$) results for the $R^* = 0$ annular duct are identical to those for the circular duct. Upon further examination, the presence of a small rectangular core at the center (say $R^* = 0.01$) significantly increases the flow resistance, fRe and Nu. Near the center, there is a big effect on the thermal flow caused by the very small core insert because of the zero velocity boundary condition on the wall. Near the outer wall the velocities are nearly identical. As stated earlier, the presence of a small rectangular core near the center ($R^* = 0.01$) significantly decreases the L_h^+. Subsequently, the L_h^+ decreases as R^* is increased.

A comparable sequence of the flow visualization photographs at two different downstream distances which confirms the numerical predictions at $Gr = 10^4$ and $Re = 500$ is given in Fig. 11. The flow visualization was made by means of a smoke generator under the steady-state condition. The steady-state condition was determined when the variation of temperature of the tube wall was less than 1% of that of its previous value. It was found that there is a good qualitative agreement between the prediction and the experiment at the same corresponding condition.

6. CONCLUSION

Numerical simulation for a steady, developing 3D laminar mixed convection in an axially uniformly heated horizontal tube with different longitudinal adiabatic inserts for a Prandtl number of 0.7 was performed by means of a finite-difference procedure with a boundary-fitted coordinate system (BFCS). The examination of flow structure, such as the onset and full development of mixed convection, in relation to thermal transport with the aid of flow visualization, and the investigation of the effects of various parameters, such as Reynolds number, Rayleigh number, aspect ratio and radius ratio of the insert on heat transfer, friction factor and entrance length in the simultaneously developing and fully developed regions, were studied extensively. Based on the results, the following conclusions can be drawn.

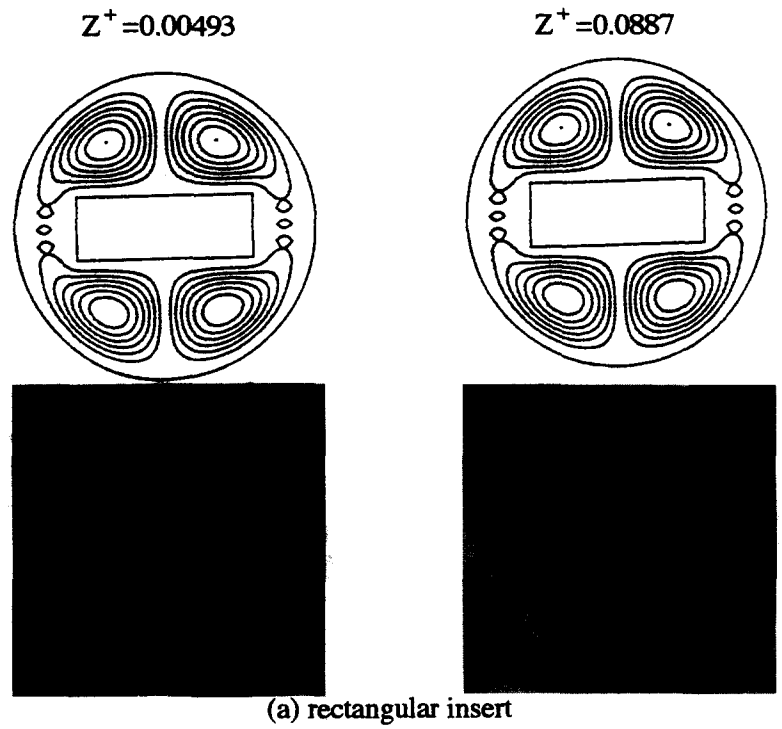

(a) rectangular insert

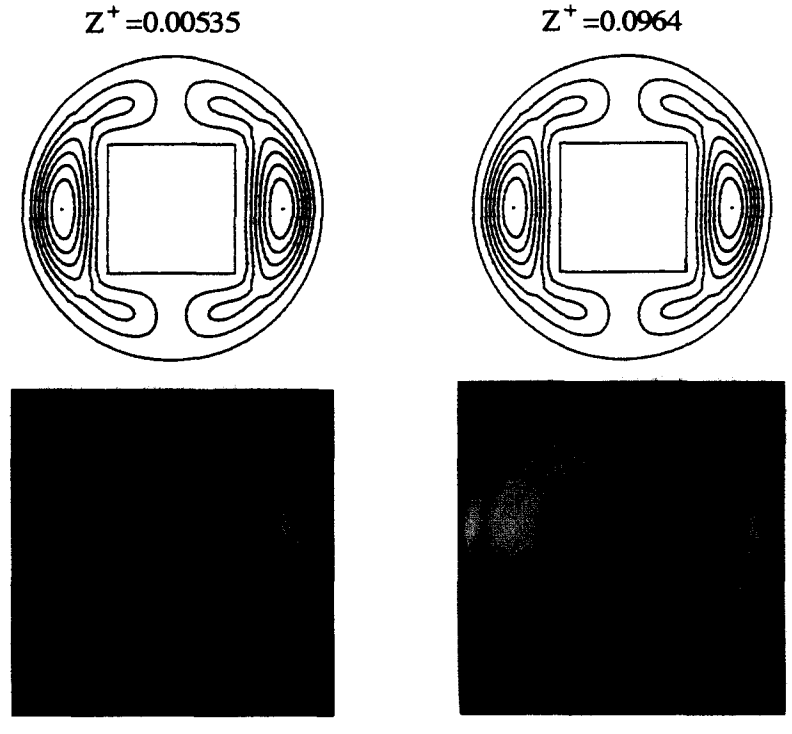

(b) square insert

Fig. 11. Comparison of the predicted flow structures for $Re = 500$ with the flow visualization at two different downstream distances.

(1) The asymmetry in the axial velocity profiles increases as R^* decreases. Moreover, near the center, the very small core tube has a large effect on the velocity profile because of the zero velocity boundary condition on the wall, while near the outer wall the profiles are nearly identical. In addition, the buoyancy

effect decelerates the fluids near the insert at locations with a small gap clearance ($R^* = 0.02$), but accelerates those at locations with a large gap clearance ($R^* = 0.4$).

(2) The average Nusselt number of each cross-section along the downstream distance decreases initially due to the growth of a thermal boundary layer and starts to rise as the secondary flow becomes more active. The effect of flow on the buoyancy force increases and decreases due to unstable stratification.

(3) The variation of L_h^+ becomes small as Gr increases, and it is roughly the same in magnitude over the whole range of Gr. In addition, for a given Gr value L_h^+ increases as Re increases. It is also seen that the L_h^+ for different Res are gradually identical as Gr increases.

(4) fRe and Nu increased and L_h^+ decreased as R^* increased until R^* equalled about 0.5, and thereafter fRe and Nu decreased as R^* increased. Moreover, it was found that the flow ($fRe = 16$) and heat transfer ($Nu_f = 4.364$) results for $R^* = 0$ annular duct are identical to those for the circular duct. In addition, the presence of a small rectangular core at the center ($R^* = 0.01$) significantly increases the flow resistance, fRe and Nu. Near the center, there is a large effect on the thermal flow caused by the very small core insert.

(5) The conventional criterion for mixed convection ($0.1 \leqslant Gr/Re^2 \leqslant 1.0$) no longer seems valid for developing flow in longitudinal heated tubes, especially with tube inserts.

Acknowledgements—This work was supported by the National Science Council of R.O.C. under Contract No. NSC 82-0401-E-110-095 and numerical results were performed on a CONVEX C3840 supercomputer at the National Sun Yat-Sen University. Special thanks go to Mr Ming-Hung Chiang for preparation of the manuscript.

REFERENCES

1. R. K. Shah and M. S. Bhatti, Laminar convection heat transfer in ducts. In *Handbook of Single-Phase Convection Heat Transfer* (Edited by S. Kakac, R. K. Shah and W. Aung), Chap. 3. Wiley, New York (1987).
2. S. C. Solanki, J. S. Saini and D. P. Gupta, An experimental investigation of fully developed laminar flow in a non-circular annulus, *Eighth National Conference on Heat Mass Transfer*, HMTA34-85, Visakhapatnam (1985).
3. S. C. Solanki, S. Prakash, J. S. Saini and C. P. Gupta, Forced convection heat transfer in doubly connected ducts, *Int. J. Heat Fluid Flow* **8,** 107–110 (1987).
4. J.-D. Chen and S.-S. Hsieh, Assessment study of longitudinal rectangular plate inserts as tubeside heat transfer augmentative device, *Int. J. Heat Mass Transfer* **34,** 2545–2553 (1991).
5. J.-D. Chen and S.-S. Hsieh, Buoyancy effect on laminar forced convection in a horizontal tube with a longitudinal thin plate insert, *Int. J. Heat Mass Transfer* **35,** 263–267 (1992).
6. S. V. Patankar, *Numerical Heat Transfer and Fluid Flow*. Hemisphere, Washington, DC (1980).
7. S. V. Patankar and D. B. Spalding, A calculation procedure for heat, mass and momentum transfer in three-dimensional parabolic flows, *Int. J. Heat Mass Transfer* **15,** 1787–1806 (1972).
8. J. F. Thompson, F. C. Thames, C. W. Mastin and S. P. Shanks, Use of numerically generated body-fitted coordinate systems for solution of the Navier–Stokes equations, *Proceeding of the AIAA Second Computational Fluid Dynamics Conference*. Hartford, CT (1975).
9. J. F. Thompson, Z. U. A. Warsi and C. W. Mastin, *Numerical Grid Generation: Foundation and Applications* (1st Edn). North-Holland, Amsterdam (1985).
10. D. V. Rao and M. S. El-Genk, Buoyancy induced instability of laminar flow in vertical annuli: II. Model development and analysis, *Int. J. Heat Mass Transfer* **33,** 2161–2172 (1990).
11. F. P. Incropera and J. A. Schutt, Numerical simulation of laminar mixed convection in the entrance region of horizontal rectangular ducts, *Numer. Heat Transfer* **8,** 707–729 (1985).
12. M. M. M. Abou-Ellail and S. M. Morcos, Buoyancy effects in the entrance region of horizontal rectangular channels, *ASME J. Heat Transfer* **105,** 924–928 (1983).
13. D. K. Choi and D. H. Chi, Developing mixed convection flow in a horizontal tube under circumferentially non-uniform heating, *Int. J. Heat Mass Transfer* **17,** 1899–1913 (1994).
14. U. Narusawa, Numerical analysis of mixed convection at the entrance region of a rectangular duct heated from below, *Int. J. Heat Mass Transfer* **36,** 2375–2384 (1993).